arXiv:0706.3741v2 [astro-ph] 24 Aug 2007

Observational Signatures of High-Energy Emission during the Shallow Decay Phase of GRB X-Ray Afterglows

Y. W. Yu[1,3], X. W. Liu[2,4], and Z. G. Dai[1]

[1]*Department of Astronomy, Nanjing University, Nanjing 210093, China;*
yuyw@nju.edu.cn, dzg@nju.edu.cn
[2]*Purple Mountain Observatory, Chinese Academy of Sciences, Nanjing 210008, China;*
xwliu@pmo.ac.cn
[3]*Institute of Astrophysics, Huazhong Normal University, Wuhan 430079, China*
[4]*National Astronomical Observatories, Chinese Academy of Sciences, Beijing 100012, China*

ABSTRACT

The widely existing shallow decay phase of the X-ray afterglows of gamma-ray bursts (GRBs) is generally accepted to be due to long-lasting energy injection. The outflows carrying the injecting energy, based on the component that is dominative in energy, fall into two possible types: baryon-dominated and lepton-dominated ones. The former type of outflow could be ejecta that is ejected during the prompt phase of a GRB and consists of a series of baryonic shells with a distribution of Lorentz factors, and the latter type could be an electron-positron-pair wind that is driven by the post-burst central engine. We here provide a unified description for the dynamics of fireballs based on these two types of energy injection, and calculate the corresponding high-energy photon emission by considering synchrotron radiation and inverse Compton scattering (including synchrotron self-Compton and combined inverse-Compton) of electrons. We find that, in the two energy-injection models, there is a plateau (even a hump) in high-energy light curves during the X-ray shallow decay phase. In particular, a considerable fraction of the injecting energy in the lepton-dominated model can be shared by the long-lasting reverse shock since it is relativistic. Furthermore, almost all of the energy of the reverse shock is carried by leptons, and thus the inverse-Compton emission is enhanced dramatically. Therefore, this model predicts more significant high-energy afterglow emission than the baryon-dominated model. We argue that these observational signatures would be used to discriminate between different energy-injection models in the upcoming *Gamma-ray Large Area Space Telescope* (GLAST) era.

Subject headings: gamma rays: bursts — radiation mechanism: nonthermal

1. Introduction

As discovered by Swift, there is a shallow decay phase (temporal indices $\alpha \sim [0, -0.8]$) from post-burst several tens of seconds to several hours (even days) occurring in the X-ray afterglow light curves of a significant fraction of gamma-ray bursts (GRBs) (Nousek et al. 2006; O'Brien et al. 2006; Willingale et al. 2007; Liang et al. 2007). This shallow decay phase is obviously beyond understanding of the standard afterglow model (Mészáros & Rees 1997; Sari et al. 1998), but is generally accepted to be due to continuous energy injection into relativistic blast waves (e.g., Zhang et al. 2006; Nousek et al. 2006; Fan & Xu 2006; Sollerman et al. 2007; de Pasquale et al. 2006, 2007). In particular, Liang et al. (2007) recently compared the closure relations derived from a simple energy-injection form, $\dot{E}_{\rm inj} \propto t^{-q}$, with the observed temporal and spectral indices of afterglows of 53 GRBs and then argued that a roughly constant injection luminosity may be favored by the observations. However, although this simple injection form is usually assumed in model fitting, the specific nature of the energy injection should be concerned and studied further.

The physical nature of an injecting energy flow discussed in the literature involves two possible candidates: (i) ejecta that consists of a series of shells with a distribution of Lorentz factors, which are dominated in energy by baryons (Rees & Mészáros 1998; Panaitescu et al. 1998; Sari & Mészáros 2000; Granot & Kumar 2006; Liu et al. 2007), and (ii) a post-burst energy flow that results from a long-lasting activity of the central engine (Dai & Lu 1998a, 1998b; Zhang & Mészáros 2001a; Wang & Dai 2001; Dai 2004; Fan & Xu 2006; Yu & Dai 2007). In the former case, the total energy carried by the ejecta is released from the central engine during the prompt phase of a GRB. Subsequently, during the afterglow phase, lower-velocity shells catch up and collide with foregoing, higher-velocity but decelerated shells continuously because of an assumed power-law distribution of Lorentz factors in the ejecta. This persistent collision leads to a long-lasting Newtonian or trans-relativistic reverse shock that propagates into the ejecta. Meanwhile, the shock-heated ejecta pushes the outward-moving relativistic blast wave and thus reduces the deceleration of the blast wave effectively, which accounts for the shallow decay. In the latter case, most of the energy that produces an afterglow is argued to be continuously released after (not during) the burst, but the GRB ejecta may provide only a relatively small amount of energy for the blast wave. Initially, the post-burst energy flow may be dominated in energy by the Poynting flux. However, as it propagates outward, the flow would evolve to an ultrarelativistic kinetic-energy flow dominated by a component of electron-positron pairs through some mechanisms (e.g., magnetic reconnection) at larger radii (Coroniti 1990; Michel 1994; Kirk & Skjæraasen 2003). It is this ultrarelativistic leptonic wind (rather than the electromagnetic flux) that feeds the blast wave and maintains a long-lasting relativistic reverse shock. The emission of the more and more energetic blast wave and the emission of the reverse shock together give rise to the shallow decay (Dai 2004). Therefore, we conclude from the above discussion that the injecting energy flows are likely to be matter-dominated. Furthermore, based on the component that is dominative in energy, the injecting flows perhaps have two types: a baryon-dominated outflow and a lepton-dominated outflow. The two corresponding representative models as described above are here called the radially structured ejecta (RSE) model (Rees & Mészáros 1998) and the relativistic wind bubble (RWB) model (Dai 2004), respectively.

In order to provide an effective test on the models mentioned above, a careful investigation of high-energy emission is important and urgent, as the launch and detection of GLAST are upcoming (Ritz 2007). In this paper, we calculate high-energy afterglow emission during the shallow decay phase of X-ray afterglows based on these two models and give corresponding observational signatures. Recently, Wei & Fan (2007), Fan et al. (2007), and Gou & Mészáros (2007) have made some attempts on high-energy afterglows. In their papers, the authors studied only the effect of the forward-shocked medium with the simple energy-injection form of $\dot{E}_{\rm inj} \propto t^{-q}$, but didn't consider the effect of the injecting flow itself. However, as found by Dai (2004), Uhm & Beloborodov (2007), Genet et al. (2007), Yu & Dai (2007), and Liu et al. (2007), the reverse shock that propagates into the injecting flow could play an important role in the emission in X-ray and/or optical bands in some situations. Therefore, high-energy emission features due to the reverse shock are also expected. In the RSE and RWB models, the high-energy photon emission from shocked materials is mainly produced by inverse Compton (IC) scattering of shock-accelerated electrons (for simplicity, electrons and positrons are not differentiated) off synchrotron seed photons (Sari & Esin 2001). Besides the synchrotron self-Compton (SSC) radiation from two shocked regions, we also consider two combined IC (CIC) processes, i.e., scattering of reverse shock photons by forward-shocked electrons and scattering of forward shock photons by reverse-shocked electrons, as pointed out by Wang, Dai & Lu (2001).

The structure of this paper is organized as follows: in the next section we provide a unified description for the dynamics of fireballs in the RSE and RWB models. In §3, we present the energy distributions of shocked electrons that are determined by the shock-acceleration effect and the synchrotron & IC cooling effect, and formulate calculations of the synchrotron and IC radiation (including SSC and CIC). In §4, we show numerical results of the dynamics, spectra and light curves for some typical parameters in the two models. Finally, in §5, a summary is given and the observability of high-energy emission by the Large Area Telescope (LAT) instrument of GLAST is discussed.

2. Dynamics

As illustrated in Figure 1, in both the RWB and RSE models, the system can be divided into four regions by the forward and reverse shocks[1]: (1) the unshocked ambient medium, (2) the forward-shocked medium, (3) the reverse-shocked materials (i.e., shocked leptonic wind for the RWB model or shocked GRB ejecta for the RSE model), and (4) the unshocked cold wind or GRB ejecta, where regions 2 and 3 are separated by a contact-discontinuity surface.

2.1. Structure of injecting flows

Figure 1 also shows illustrative Γ_i-distributions in all the regions. The main differences between the two models are in the structure and composition of injecting flows:

(i) *The RWB model.* Following the analysis of Dai (2004) for a magnetar-driven wind, we simply assume that the leptonic wind propagates outward with a constant luminosity $L_{\rm w}$ and a constant bulk Lorentz factor $\Gamma_{\rm w}$ during a period of $T_{\rm w}$ after the burst[2]. Thus, we can calculate the number density ($n'^{(\rm RWB)}_4$) and the bulk Lorentz factor ($\Gamma^{(\rm RWB)}_4$) of the pre-shock materials at the reverse shock front as

$$n'^{(\rm RWB)}_4 = n'_{\rm w}(R) = \frac{L_{\rm w}}{4\pi R^2 \Gamma_{\rm w}^2 m_{\rm e} c^3}, \tag{1}$$

$$\Gamma^{(\rm RWB)}_4 = \Gamma_{\rm w}, \tag{2}$$

where $m_{\rm e}$ is the rest mass of electrons and R is the radius of the system in the thin shell approximation.

(ii) *The RSE model.* As suggested by Rees & Mészáros (1998), the mass distribution in the wide GRB ejecta associated with a distribution of bulk Lorentz factors reads

---

[1] It takes only a short time (tens to hundreds of seconds) for a reverse shock to cross the ejecta of a typical GRB in the RWB model. Meanwhile, two forward shocks forming initially during the interaction of the ejecta both with the medium and with the leptonic wind are assumed to merge to one forward shock. In addition, the contribution of the GRB ejecta to the afterglow emission should be negligible as compared with the shocked medium and the shocked wind during the emission period of our interest. Thus, for simplicity, the structure of an RWB can be described approximately by Figure 1(a). However, for the RSE model, the situation is different. The reverse shock propagates into the GRB ejecta for a long time and thus influences the afterglow emission during the first hours significantly (see numerical calculations in §4).

[2] A quantity Q' with a prime is measured in the comoving frame of a certain region, while the other quantities Qs are measured in the local medium's rest frame except for specific declarations. In addition, a subscript "$i = 1, 2, 3, 4$" represents a quantity describing region "i".

$$M_{\rm ej}(>\Gamma_{\rm ej}) \propto \Gamma_{\rm ej}^{-s}. \tag{3}$$

Moreover, we assume that the $\Gamma_{\rm ej}$-distribution in the GRB ejecta satisfies

$$\Gamma_{\rm ej}(x) \propto x^{-1/b}, \tag{4}$$

where x is the displacement of the reverse shock propagating into the ejecta. If the Lorentz factor of the end of the ejecta (i.e., the minimum bulk Lorentz factor) is denoted by $\Gamma_{\rm ej,min}$, then the total displacement of the reverse shock when it crosses the ejecta could be estimated as $R_{\rm cross}/2\Gamma^2_{\rm ej,min} \sim 10^{13} - 10^{14}$ cm. Under these assumptions, the associated injecting energy distributes with respect to x as $E_{\rm ej} \propto x^{s/b}$, and $n'^{(\rm RSE)}_4$ and $\Gamma^{(\rm RSE)}_4$ are given by

$$n'^{(\rm RSE)}_4 = n'_{\rm ej}(x) = \frac{dM_{\rm ej}/dx}{4\pi R^2 \Gamma_{\rm ej}(x) m_{\rm p}}, \tag{5}$$

$$\Gamma^{(\rm RSE)}_4 = \Gamma_{\rm ej}(x), \tag{6}$$

where $m_{\rm p}$ is the proton rest mass.

2.2. Dynamic equations

Now, we describe the dynamic evolution of the systems under the effect of the two types of injecting flow. A resultant long-lasting reverse shock transforms the injecting energy into the internal energy of the reverse-shocked materials continuously. Meanwhile, a part of fresh energy is further transformed to the kinetic energy ($E_{\rm K,2}$) of region 2 through the work done by region 3: $\delta W = 4\pi P'_3 R^2 dR$, where P'_3 is the pressure of region 3. Then, we have

$$\delta W = dE_{\rm K,2} = d\left[(\Gamma_2^2 - 1) M_{\rm sw} c^2\right], \tag{7}$$

where $M_{\rm sw}$ is the rest mass of the swept-up medium and Γ_2 is the average bulk Lorentz factor of the shocked medium. Thus, the dynamic evolution of region 2 is described by (Dai 2004)

$$\frac{d\Gamma_2}{dR} = \frac{4\pi R^2\left[P'_3/c^2 - (\Gamma_2^2 - 1) n_1 m_{\rm p}\right]}{2\Gamma_2 M_{\rm sw}}, \tag{8}$$

where $dM_{\rm sw}/dR = 4\pi R^2 n_1 m_{\rm p}$ is applied and n_1 is the proton number density of the ambient medium. To integrate the above equation, the pressure of region 3 should be calculated by

$$P'_3 = \frac{1}{3}(\Gamma'_{34} - 1)(4\Gamma'_{34} + 3) n'_4 m_{\rm re} c^2, \tag{9}$$

where $\Gamma'_{34} = \Gamma_3\Gamma_4(1-\beta_3\beta_4)$ is the Lorentz factor of region 3 measured in region 4 and β_i is the velocity in units of c, and $m_{\rm re}$ represents the electron and proton rest masses for the RWB and RSE models, respectively. The evolution of Γ_3 can be obtained from the equality of Lorentz factors of the two sides of the contact discontinuity surface, assuming that the shocked medium in region 2 satisfies the adiabatic self-similar solution of Blandford & McKee (1976)

$$\Gamma_3 = \Gamma_2\chi^{-1/2}. \tag{10}$$

To fix the self-similar variable χ, we use the following relationship,

$$P'_3 = \frac{4}{3}\Gamma_2^2 n_1 m_{\rm p} c^2 \chi^{-17/12}. \tag{11}$$

Combining Eqs. 9, 10, and 11 to eliminate χ, we can solve Γ_3 and P'_3 as functions of Γ_2 and thus integrate Eq. 8. Furthermore, the rest mass of region 3 is obtained from

$$\frac{dM_3}{dR} = 4\pi R^2(\beta_4-\beta_{\rm RS})\Gamma_4 n'_4 m_{\rm re}, \tag{12}$$

where $\beta_{\rm RS} = (\Gamma_3 n'_3\beta_3 - \Gamma_4 n'_4\beta_4)/(\Gamma_3 n'_3 - \Gamma_4 n'_4)$ is the velocity of the reverse shock.

When the reverse shock crosses the wind or GRB ejecta, the dynamic evolution of region 3 is described by Kobayashi & Sari (2000) and Kobayashi (2000). Then, the pressure of region 3 in Eq. 8 decreases significantly and thus is negligible. As a result, the dynamic equation of region 2 returns to the form of the standard afterglow model in Huang et al. (1999).

3. Electron distributions and emission mechanisms

After the dynamic evolution equations are given, the internal physics of the shocked regions in the RWB and RSE models can be considered as follows.

3.1. Electron energy distributions

As the forward and reverse shocks propagate, the bulk kinetic energies of the shells are gradually transformed into the internal energy of the shocked materials, the density of which is denoted by e'_i. The internal energy will be partially carried by the accelerated electrons and magnetic fields, the energy densities of which are factions $\epsilon_{{\rm e},i}$ and $\epsilon_{{\rm B},i}$ of e'_i, respectively. Through the shock acceleration, the electrons behind the forward/reverse shock will obtain an initial energy distribution $N'_{{\rm ini},i}(\gamma'_i) \propto \gamma'^{-p}_i$ with the minimum Lorentz

factor ${\gamma'}_{\mathrm{m},i} = \lambda_i[(p-2)/(p-1)]\epsilon_{\mathrm{e},i}(\tilde{\Gamma}_i - 1)$ and the maximum Lorentz factor $\gamma'_{\mathrm{max},i} \approx 10^8[B'_i(1+Y_i)]^{-1/2}$, where $\lambda_2 = m_{\mathrm{p}}/m_{\mathrm{e}}$, $\lambda_3 = m_{\mathrm{re}}/m_{\mathrm{e}}$, $\tilde{\Gamma}_2 = \Gamma_2$, $\tilde{\Gamma}_3 = \Gamma'_{34}$, and B'_i is the magnetic field strength. The occurrence of the Compton parameter Y_i is induced by the IC cooling effect. By considering the cooling effect of the synchrotron and IC radiation, we can obtain the actual electron energy distributions (Huang et al. 2000):
for ${\gamma'}_{\mathrm{c},i} \le {\gamma'}_{\mathrm{m},i}$,

$$N'_i({\gamma'}_i) \propto \left\{ \begin{array}{ll} {\gamma'}_i^{-2} & \text{if } \; {\gamma'}_{\mathrm{c},i} \le {\gamma'}_i \le {\gamma'}_{\mathrm{m},i}, \\ {\gamma'}_i^{-p-1} & \text{if } \; {\gamma'}_{\mathrm{m},i} < {\gamma'}_i \le {\gamma'}_{\mathrm{max},i}; \end{array} \right. \tag{13}$$

and for ${\gamma'}_{\mathrm{c},i} > {\gamma'}_{\mathrm{m},i}$,

$$N'_i({\gamma'}_i) \propto \left\{ \begin{array}{ll} {\gamma'}_i^{-p} & \text{if } \; {\gamma'}_{\mathrm{m},i} \le {\gamma'}_i \le {\gamma'}_{\mathrm{c},i}, \\ {\gamma'}_i^{-p-1} & \text{if } \; {\gamma'}_{\mathrm{c},i} < {\gamma'}_i \le {\gamma'}_{\mathrm{max},i}. \end{array} \right. \tag{14}$$

The cooling Lorentz factor ${\gamma'}_{\mathrm{c},i}$ is defined by equaling the cooling timescale and dynamic expansion timescale of the system, and it reads

$${\gamma'}_{\mathrm{c},i} = \frac{6\pi m_{\mathrm{e}} c}{(1+Y_i)\sigma_{\mathrm{T}}\Gamma_i {B'}_i^2 t} \tag{15}$$

with σ_{T} being the Thomson scattering cross section. Here, the dynamic timescale measured in the observer's frame in calculating ${\gamma'}_{\mathrm{c}}$ is assumed to be approximately equal to the observer's time t since the trigger. In addition, the self-absorption of the synchrotron photons is ignored in Eqs. 13 and 14 for the high-energy emission that we are interested in. Following Sari & Esin (2001), the Compton parameter Y_i in Eq. 15, defined as the ratio of the IC (including SSC and CIC) luminosity to the synchrotron luminosity of electrons, is estimated by

$$Y_2 \equiv \frac{L'_{\mathrm{IC},2}}{L'_{\mathrm{syn},2}} = \frac{U'_{\mathrm{syn},2} + \frac{1}{2}U'_{\mathrm{syn},3}}{U'_{\mathrm{B},2}}, \tag{16}$$

$$Y_3 \equiv \frac{L'_{\mathrm{IC},3}}{L'_{\mathrm{syn},3}} = \frac{U'_{\mathrm{syn},3} + \frac{1}{2}U'_{\mathrm{syn},2}}{U'_{\mathrm{B},3}}, \tag{17}$$

where $U'_{\mathrm{syn},i} = \eta_i\epsilon_{\mathrm{e},i}e'_i/(1+Y_i)$ and $U'_{\mathrm{B},i} = \epsilon_{\mathrm{B},i}e'_i$ are the energy densities of synchrotron seed photons and magnetic fields, respectively. The radiation efficiency η_i reads

$$\eta_i = \left\{ \begin{array}{ll} 1, & \text{for } \; {\gamma'}_{\mathrm{c},i} \le {\gamma'}_{\mathrm{m},i}, \\ ({\gamma'}_{\mathrm{c},i}/{\gamma'}_{\mathrm{m},i})^{2-p}, & \text{for } \; {\gamma'}_{\mathrm{c},i} > {\gamma'}_{\mathrm{m},i}. \end{array} \right. \tag{18}$$

A factor of $\frac{1}{2}$ in Eqs. 16 and 17 occurs, because only about one-half of seed photons from one shocked region will diffuse into the other one for the CIC process. In two extreme situations,

equations 16 and 17 can be simplified as
i) for $U'_{\rm syn,3} \gg U'_{\rm syn,2}$,

$$Y_2 = \eta_3 \frac{\epsilon_{\rm e,3} e'_3}{2\epsilon_{\rm B,2} e'_2}(1+Y_3)^{-1}, \quad Y_3 = \eta_3 \frac{\epsilon_{\rm e,3}}{\epsilon_{\rm B,3}}(1+Y_3)^{-1}; \tag{19}$$

ii) for $U'_{\rm syn,3} \ll U'_{\rm syn,2}$,

$$Y_2 = \eta_2 \frac{\epsilon_{\rm e,2}}{\epsilon_{\rm B,2}}(1+Y_2)^{-1}, \quad Y_3 = \eta_2 \frac{\epsilon_{\rm e,2} e'_2}{2\epsilon_{\rm B,3} e'_3}(1+Y_2)^{-1}. \tag{20}$$

3.2. SSC and CIC emission

Once the electron distribution is known, the synchrotron emissivity of electrons in region i at frequency ν' is calculated directly by (Rybicki & Lightman 1979)

$$\varepsilon'^{\rm syn}_i(\nu') = \frac{\sqrt{3} q_{\rm e}^3 B'_i}{m_{\rm e} c^2} \int d\gamma'_i N'_i(\gamma'_i) \mathcal{F}\left(\frac{\nu'}{\nu'_{\rm c}}\right), \tag{21}$$

where $q_{\rm e}$ is the electron charge, $\nu'_{\rm c} = 3\gamma'^2_i q_{\rm e} B'_i/(4\pi m_{\rm e} c)$, $\mathcal{F}(u) = u\int_u^\infty K_{5/3}(k)dk$, and $K_{5/3}(k)$ is the Bessel function.

Accompanying with the synchrotron radiation, the electrons also lose their energy through upscattering the synchrotron seed photons. As usual, the first-order IC scattering is considered and the higher-order processes are neglected. According to Blumenthal & Gould (1970), when the Klein-Nishina suppression is considered, the IC emissivity (at a frequency ν') of electrons in region i upscattering seed photons from region j is calculated by ($i = j$ for SSC and $i \neq j$ for CIC)

$$\varepsilon'^{\rm IC(j)}_i(\nu') = 3\sigma_{\rm T} \int d\gamma'_i N'_i(\gamma'_i) \int d\nu^\dagger_j \frac{\nu' f^\dagger_j}{4\gamma'^2_i \nu^{\dagger 2}_j} g(x,y), \tag{22}$$

where $g(x,y) = 2y\ln y + (1+2y)(1-y) + \frac{1}{2}\frac{x^2y^2}{1+xy}(1-y)$ with $x = 4\gamma'_i h\nu^\dagger_j/m_{\rm e}c^2$, $y = h\nu'/[x(\gamma'_i m_{\rm e}c^2 - h\nu')]$. $\nu^\dagger_j$ and $f^\dagger_j$ are the frequency and the corresponding flux density of the incident photons from region j, respectively, which are measured in the comoving frame of region i.

The observed synchrotron and IC flux densities at a frequency ν (measured in the observer's frame) from region i are given respectively by (Huang et al. 2000)

$$F^{\rm syn}_{\nu,i}(t) = \int_0^\pi d\theta V'_i \frac{\sin\theta}{2} \frac{\varepsilon'^{\rm syn}_i(\mathcal{D}_i\nu)}{4\pi D_{\rm L}^2 \mathcal{D}_i^3}, \tag{23}$$

$$F_{\nu,i}^{\mathrm{IC}(j)}(t) = \int_0^\pi d\theta V_i' \frac{\sin\theta}{2} \frac{\varepsilon_i'^{\mathrm{IC}(j)}(\mathcal{D}_i\nu)}{4\pi D_{\mathrm{L}}^2 \mathcal{D}_i^3}, \tag{24}$$

where D_{L} is the luminosity distance and $\mathcal{D}_i = \Gamma_i(1-\beta_i\cos\theta)$ is the Doppler factor. Here, the viewing angle is assumed to be zero and θ is the angle between the moving direction of the emitting material and the line of sight. The volumes V_i' of the shocked regions in Eqs. 23 and 24 are functions of θ because the integrations are performed over the equal-arrival surface. In addition, the jet correction should be considered if the GRB ejecta is collimated.

4. Numerical Results

4.1. Dynamic evolution

For the RWB and RSE models, we first calculate the dynamic evolution with radius. The initial value of R is taken to be $\sim 10^{16}$ cm as the deceleration radius. For the RWB model, as in Yu & Dai (2007), the isotropic wind luminosity is $L_{\mathrm{w}} = 4\times10^{47}B_{14}^2$ erg s^{-1}, the wind duration $T_{\mathrm{w}} = 5\times10^4 B_{14}^{-2}$ s, and the bulk Lorentz factor of the wind $\Gamma_{\mathrm{w}} = 10^4$, where B_{14} is the magnetic field strengthen of the central magnetar in unit of 10^{14} G. Here, we take $B_{14} = 4$ for a typical magnetar. Thus the total energy of the wind is $E_{\mathrm{w}} = 2.0\times10^{52}$ erg. However, the isotropic kinetic energy of the previous GRB ejecta is relatively small, $E_{\mathrm{ej}}^{\mathrm{RWB}} = 10^{51}$ erg. For consistency, we assume that, in the RSE model, the isotropic kinetic energy carried by the wide GRB ejecta is $E_{\mathrm{ej}}^{\mathrm{RSE}} = 2.1\times10^{52}$ erg, and the distribution-related parameters are $\Gamma_{\mathrm{ej,min}} = 30$, $\Gamma_{\mathrm{ej,max}} = 500$, and $s = b = 1.5$. In addition, the number density of the ambient interstellar medium is $n_1 = 1$ cm^{-3} in both cases.

The dotted lines in Figure 2 represent the dynamic evolution of blast waves with a certain energy (i.e., without energy injection), and the solid lines show the energy injection case. We can see clearly from this figure that the energy ($\propto \Gamma_2^2$) of the shocked medium increases gradually until the energy injection is over. As analyzed in Yu & Dai (2007), the final energy carried by the shocked medium is a fraction $\sim 67\%$ of the total injecting energy for the RWB model versus $\sim 90\%$ for the RSE model. Meanwhile, the other fraction of the injecting energy ($\sim 33\%$ and $\sim 10\%$ for the RWB and RSE models, respectively) should be shared by the reverse-shocked material. In addition, we can know that the reverse shock is relativistic in the RWB model, but Newtonian or trans-relativistic in the RSE model, according to an estimation of the Lorentz factor of region 3 relative to region 4 from

$$\Gamma_{34}' \approx \frac{1}{2}\left(\frac{\Gamma_3}{\Gamma_4} + \frac{\Gamma_4}{\Gamma_3}\right) \tag{25}$$

with the values of Γ_3 as shown in Figure 2. This difference between the reverse shocks in the two models is just the reason why the reverse shock in the RWB model can share more injecting energy than the one in the RSE model.

4.2. Spectra and light curves

To calculate the emission of shocked materials, we take the microphysical parameters $p = 2.3$ and $\epsilon_{\rm B} = 0.01$ for all shocked regions. Then, $\epsilon_{\rm e}$ is calculated by $\sqrt{\epsilon_{\rm B}}$ for the baryon-dominated regions (i.e., regions 2 & 3 in the RSE model and region 2 in the RWB model) as argued by Medvedev (2006) and $(1-\epsilon_{\rm B})$ for the lepton-dominated region (i.e., region 3 in the RWB model). The luminosity distance of a GRB is taken to be $D_{\rm L} = 1$ Gpc, corresponding to a redshift of 0.2.

Figure 3 shows the light curves of an RWB. From this figure, we obtain the following results. First, the shallow decay phase of an X-ray (keV) afterglow is produced during the early hours (left upper panel), which is mildly dominated by the reverse shock emission (for a detailed discussion see Yu & Dai 2007). The synchrotron radiation is the dominative mechanism in this band. Second, an obvious hump accompanying with the X-ray plateau occurs in a high-energy (MeV & GeV) afterglow, which is dominated by the IC (especially SSC) emission from the reverse-shocked wind. Finally, a comparison of light curves in different bands (right lower panel) shows that the high-energy (especially GeV) emission flux is mildly or even significantly higher than the one in X-ray band. This feature is also implied obviously by the spectra as shown in Figure 4. The peak flux of the IC emission at ~ 1 GeV is about one order of magnitude higher than the synchrotron peak at ~ 10 eV. Moreover, the IC component is dominative above sub-MeV and, in all bands, the emission from the reverse-shocked wind is more important than the one from the forward-shocked medium at 1000 s.

The results for the RSE model are shown in Figures 5 and 6. From these two figures, we find that, first, the X-ray shallow decay phase during the early hours is also produced in this model as shown in left upper panel of Figure 5, which is dominated by the forward shock. Second, the high-energy afterglow light curves also have a flattening segment. However, differing from the RWB model, the contribution to the high-energy plateau from the IC emission plays a role only in GeV band, whereas the MeV emission is totally contributed by the synchrotron mechanism during the total afterglow phase. This result arises from the relative weakness of the IC component in the RSE model as shown in Figure 6. Therefore, the flux in MeV or GeV band is lower than or approximately equal to the X-ray flux as shown in right lower panel of Figure 5. In addition, Figure 6 shows that the contribution of the emission from the reverse-shocked ejecta is negligible in all bands for the parameters that we adopt.

In conclusion, we obtain very different high-energy afterglows in the RWB and RSE models with a same amount of injecting energy that gives rise to similar X-ray afterglows. The RWB model predicts more significant (about one order of magnitude stronger) high-energy emission than the RSE model. The reasons for this difference are that the reverse shock in the RWB model is relativistic and that the energy of the reverse shock is almost totally carried by electrons. The former reason enables the reverse shock to share more (i.e., 33% vs 10%) injecting energy as discussed in Sect. 4.1, and the latter reason dramatically increases the emission efficiency of the reverse-shocked material through the enhanced IC emission. Therefore, a higher fraction of injecting energy can be radiated from the shocked regions in the RWB model. In the baryon-dominated injection model, however, this significant enhanced IC component doesn't happen even if the emission flux from the reverse shock exceeds the one from the forward shock under some extreme conditions, because most of the injecting energy in both shocked regions is locked in the baryons whose emission is weak. Therefore, we argue that the difference in high-energy emission between the RWB and RSE models is essentially due to the physical distinction between the two types of energy injection. Thus, reasonable variations of the parameters for the models should not change our results significantly.

5. Summary and discussion

The discovered shallow decay phase of GRB X-ray afterglows suggests long-lasting energy injection into relativistic blast waves. The injecting flow is likely to be dominated in energy by the component of either baryons or leptons. In this paper, we first provide a unified description for dynamics and radiation in two representative models, i.e., the RSE and RWB models. Through maintaining a long-lasting reverse shock and doing work to forward-shocked medium, both types of energy injection can produce the flattening segment in X-ray afterglow light curves easily. Second, we pay attention to calculations of the simultaneous high-energy emission that is due to synchrotron and, especially, IC (including SSC and CIC processes) radiation from the shocked materials. Our results show that, during the shallow decay phase of X-ray afterglows, there is a plateau (even a hump) in high-energy light curves in both the RSE and RWB models. As argued by Wei & Fan (2007), we suggest that the plateau/hump might account for the delayed high-energy emission of some bursts such as GRB 940217.

We also find that the high-energy emission derived from the two models has different observable features, e.g., morphologies of the light curves and spectra. In particular, more significant high-energy emission is predicted by the RWB model, because more injecting energy in this model is carried by electrons and thus the IC scattering is enhanced significantly. This difference in high-energy emission between the two models could be tested in the upcoming GLAST era. As proposed by Zhang & Mészáros (2001b) and Gou & Mészáros (2007), the fluence threshold of the LAT instrument aboard GLAST for an effective observation time $t_{\rm eff}$ in an observation energy band centered around a photon energy E is estimated by $F_{\rm thr} \sim [\Phi_0(T/t_{\rm eff})^{1/2}]Et_{\rm eff}$, where the flux sensitivity, $[\Phi_0(T/t_{\rm eff})^{1/2}]$, scales as $t_{\rm eff}^{-1/2}$ due to a limitation by the background for a long-time observation and Φ_0 is the sensitivity over an exposure time T. Specifically, over a one-year exposure period, the sensitivity above 100 MeV is $\sim 1.33\times10^{-9}$ ph s^{-1} cm^{-2} for point-source observations of GRB afterglows (Gou & Mészáros 2007). On the other hand, for a short-time observation, the fluence threshold is instead calculated by $F_{\rm thr} = 5E/A_{\rm eff}$ with the assumption that at least 5 photons are collected on an effective area $A_{\rm eff}$ of the instrument. Taking $E = 400$ MeV and $A_{\rm eff} = 6000$ cm^{-2}, we obtain the fluence threshold of GLAST LAT,

$$F_{\rm thr} = \begin{cases} 5.3\times10^{-7} \quad\quad \text{erg cm}^{-2}, & t \le 2.43\times10^4\,\text{s}, \\ 3.4\times10^{-9}t^{1/2}\ \text{erg cm}^{-2}, & t > 2.43\times10^4\,\text{s}, \end{cases} \tag{26}$$

where an observation efficiency $\eta \equiv t_{\rm eff}/t = 0.5$ due to the occultation by the earth is considered. With this fluence threshold, the observability of high-energy emission in the RWB and RSE models by GLAST LAT is shown in Figure 7. It can be seen that both the high-energy emissions predicted by the two models can be detected by GLAST LAT for the given parameters. The partial fluence of the high-energy emission in the RWB model is about an order of magnitude higher than that in the RSE model for a same amount of injecting energy. Here, the partial fluence is defined as an integration of the flux density (F_ν) over the GLAST LAT energy band [20 MeV, 300 GeV] and the time intervals $[0.5t, t]$ as done in Gou & Mészáros (2007).

Although the detection of the RWB model by GLAST LAT is obviously easier, joint observations of GLAST and Swift are necessary to distinguish between the RWB and RSE models. Simultaneous observations of a high-energy afterglow by GLAST LAT and an X-ray afterglow by Swift XRT for a same GRB could provide a ratio of fluxes (νF_ν) in the high-energy band to the X-ray. As implied by the right lower panels of Figures 3 and 5, for example, the injecting flow could be dominated in energy by baryons if the ratio $(\nu F_\nu)_{\rm GeV}/(\nu F_\nu)_{\rm keV}$ is close to 1. On the other hand, if the ratio is significantly higher than 1, there could be lepton-dominated energy injection.

Acknowledgements

We would like to thank Lijun Gou and an anonymous referee for valuable comments and suggestions that have helped us to improve an earlier version of this manuscript. This work is supported by the National Natural Science Foundation of China (grant no. 10221001 and 10640420144). YWY is also supported by the Visiting PhD Candidate Foundation of Nanjing University and the National Natural Science Foundation of China (grant no.10603002).

REFERENCES

Blandford, R. D., & McKee, C. F. 1976, Phys. Fluids., 19, 1130

Blumenthal, G. R., & Gould, R. J. 1970, Rev. Mod. Phys., 42, 237

Coroniti, F. V. 1990, ApJ, 349, 538

Dai, Z. G. 2004, ApJ, 606, 1000

Dai, Z. G., & Lu, T. 1998a, A&A, 333, L87

Dai, Z. G., & Lu, T. 1998b, Phys. Rev. Lett., 81, 4301

de Pasquale, M., et al. 2006, MNRAS, 365, 1031

de Pasquale, M., et al. 2007, accepted by MNRAS, arXiv:astro-ph/0703447

Fan, Y. Z., & Xu, D. 2006, MNRAS, 372, L19

Fan, Y. Z., Piran, T., Narayan, R., & Wei, D. M., 2007, submitted to MNRAS, arXiv:0704.2063

Genet, F., Daigne, F., & Mochkovitch, R. 2007, arXiv:astro-ph/0701204

Gou, L. J., & Mészáros, P. 2007, accepted by ApJ, arXiv:0705.1545

Granot, J., & Kumar, P., 2006, MNRAS, 366, L13

Huang, Y. F., Dai, Z. G., & Lu, T. 1999, MNRAS, 309, 513

Huang, Y. F., Gou, L. J., Dai, Z. G. & Lu, T. 2000, ApJ, 543, 90

Kirk, J. G., & Skjæraasen, O. 2003, ApJ, 591, 366

Kobayashi, S. 2000, ApJ, 545, 807

Kobayashi, S., & Sari, R. 2000, ApJ, 542, 819

Liang, E. W., Zhang, B. B., & Zhang, B. 2007, accepted by ApJ, arXiv:0705.1373

Liu, X. W., Wu, W. F., Zou, Y. C., & Lu, T. 2007, to be submitted

Medvedev, M. V. 2006, ApJ, 651, L9

Mészáros, P., & Rees, M. J. 1997, ApJ, 476, 232

Michel, F. C. 1994, ApJ, 431, 397

Nousek, J. A., et al. 2006, ApJ, 642, 389

O'Brien, P. T., et al. 2006, ApJ, 647, 1213

Panaitescu, A., Mészáros, P., & Rees, M. J. 1998, ApJ, 503, 314

Rees, M. J., & Mészáros, P. 1998, ApJ, 496, L1

Ritz, S. 2007, a review talk in the First GLAST Symposium (5 February 2007)

Rybicki, G. B., & Lightman, A. P. 1979, Radiative Processes in Astrophysics (New York: Wiley)

Sari, R., & Esin, A. A. 2001, ApJ, 548, 787

Sari, R., Piran, T., & Narayan, R. 1998, ApJ, 497, L17

Sari, R., & Mészáros, P. 2000, ApJ, 535, L33

Sollerman, J., et al. 2007, A&A, 466, 839

Uhm, Z. L., & Beloborodov, A. M. 2007, ApJ, 665, L93

Wang, W., & Dai, Z. G. 2001, Chin. Phys. Lett., 18, 1153

Wang, X. Y., Dai, Z. G., & Lu, T., 2001, ApJ, 556, 1010

Wei, D. M., & Fan, Y. Z. 2007, ChJAA, 7, 509

Willingale, R., et al. 2007, ApJ, 662, 1093

Yu, Y. W., & Dai, Z. G. 2007, A&A, 470, 119

Zhang, B., et al. 2006, ApJ, 642, 354

Zhang, B., & Mészáros, P. 2001a, ApJ, 552, L35

Zhang, B., & Mészáros, P. 2001b, ApJ, 559, 110

This preprint was prepared with the AAS LaTeX macros v5.2.

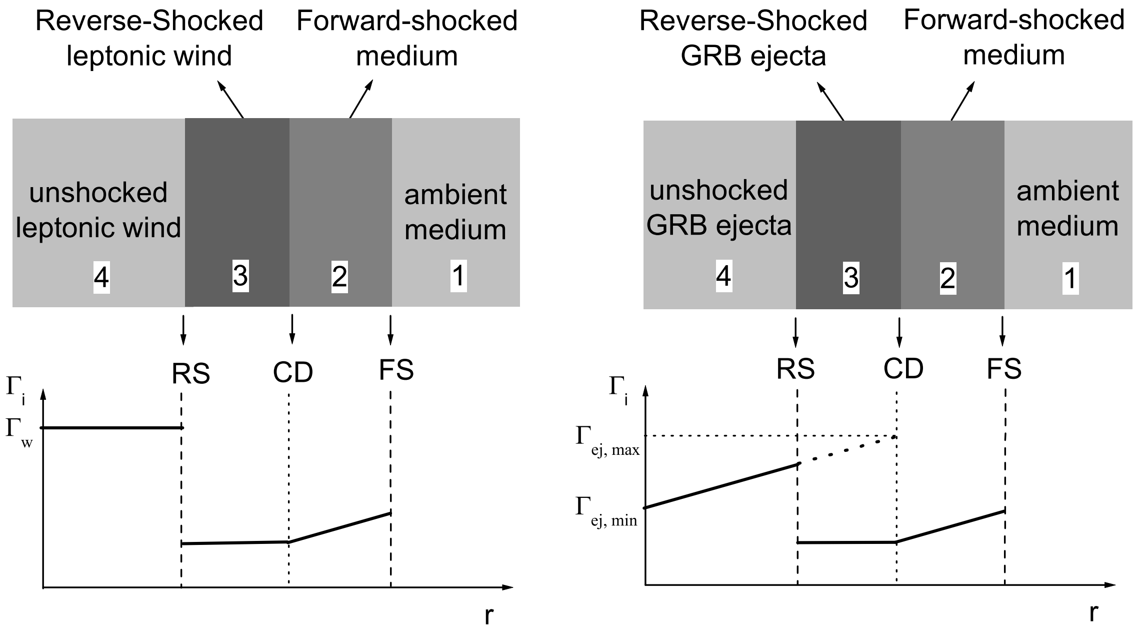

(a) RWB model

(b) RSE model

Fig. 1.— Illustrations of four regions divided by the forward and reverse shocks in the RWB (left) and RSE (right) models, and the corresponding distributions of Lorentz factors (not scaled).

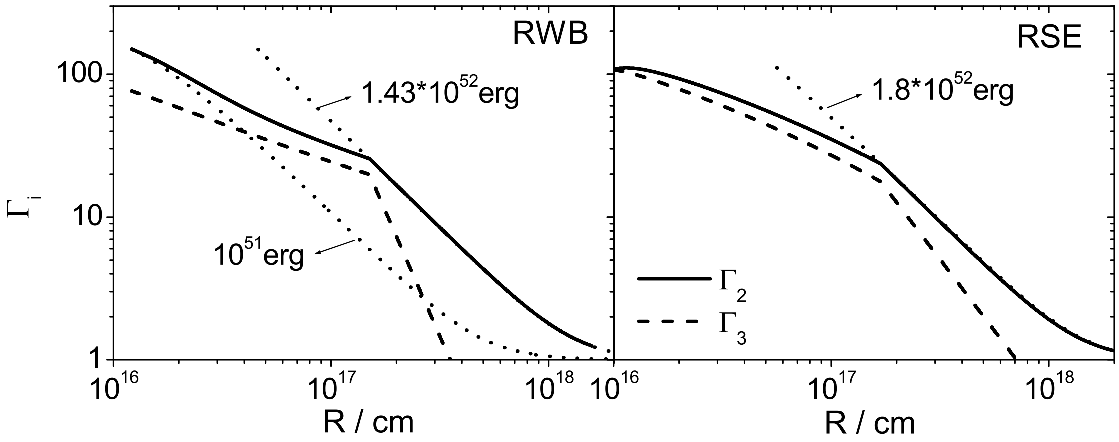

Fig. 2.— Evolution of the Lorentz factors of regions 2 and 3 as the shells in the RWB (left) and RSE (right) models expand. A dotted line represents the dynamic evolution of the shell with a fixed amount of energy as labeled.

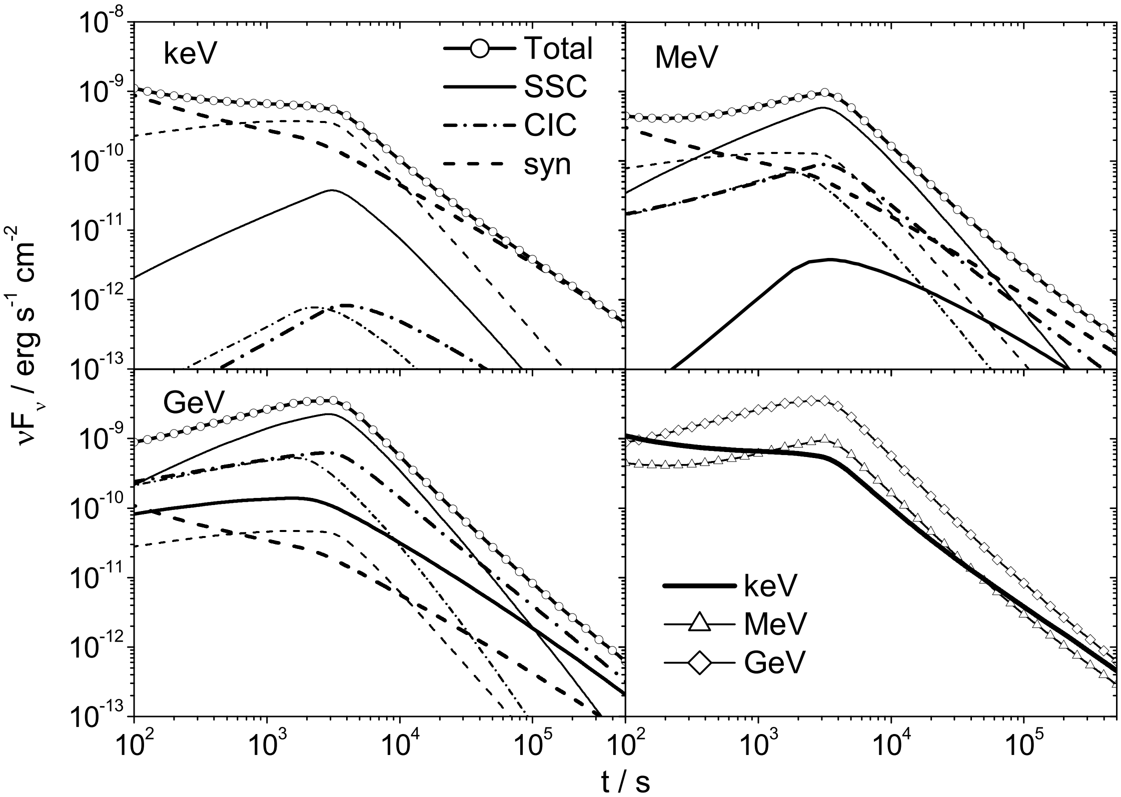

Fig. 3.— Light curves in X-ray (keV) and high energy gamma-ray (MeV, GeV) bands for the RWB model. The emission from the forward-shocked medium is represented by thick lines, while the reverse shock corresponds to thin lines. The solid, dash-dotted, and dashed lines are due to SSC, CIC, and synchrotron processes, respectively.

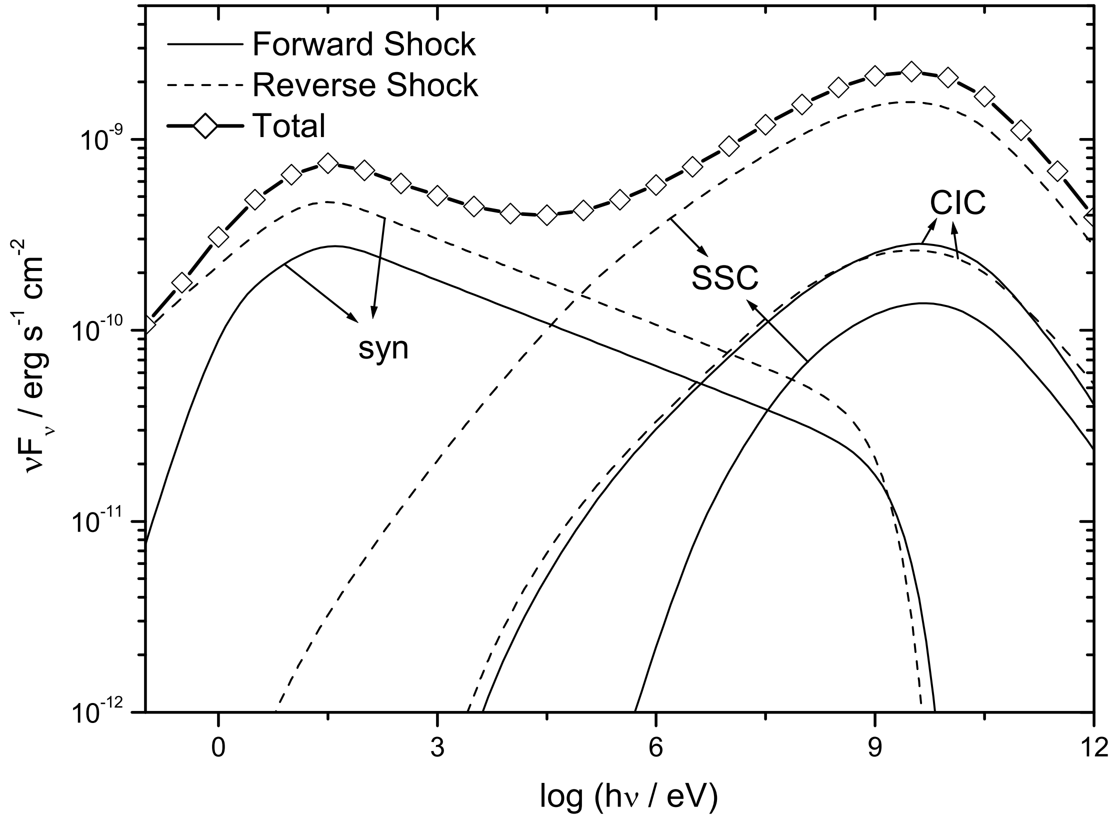

Fig. 4.— Synchrotron and IC spectra at 1000 s for the RWB model. The solid lines represent the emission contributed by the forward-shocked medium, while the dotted lines correspond to the reverse-shocked wind.

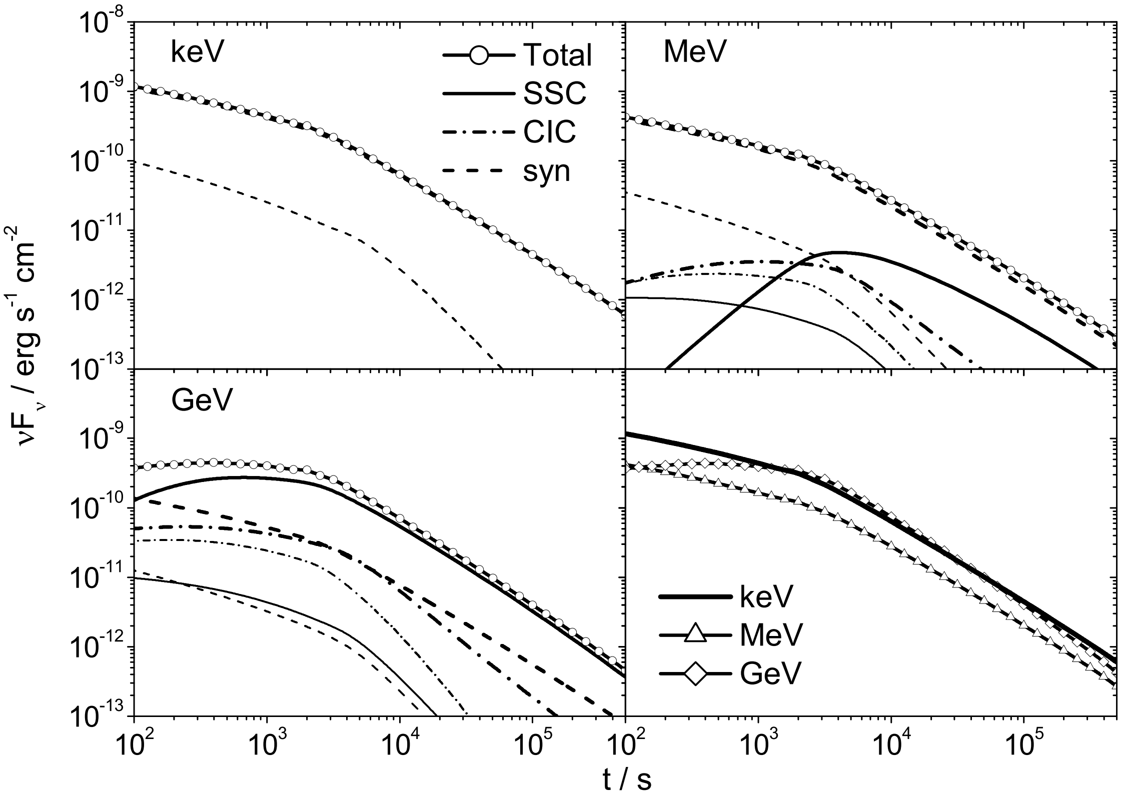

Fig. 5.— Same as in Figure 3 but for the RSE model.

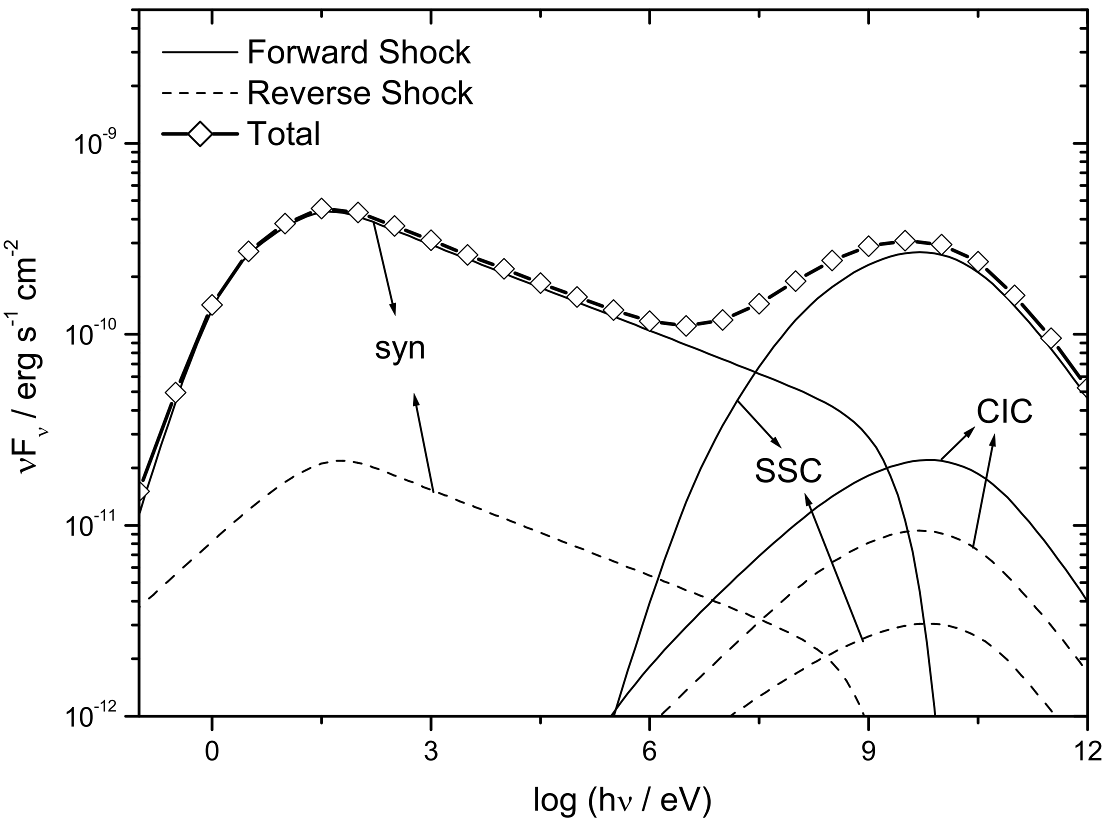

Fig. 6.— Same as in Figure 4 but for the RSE model.

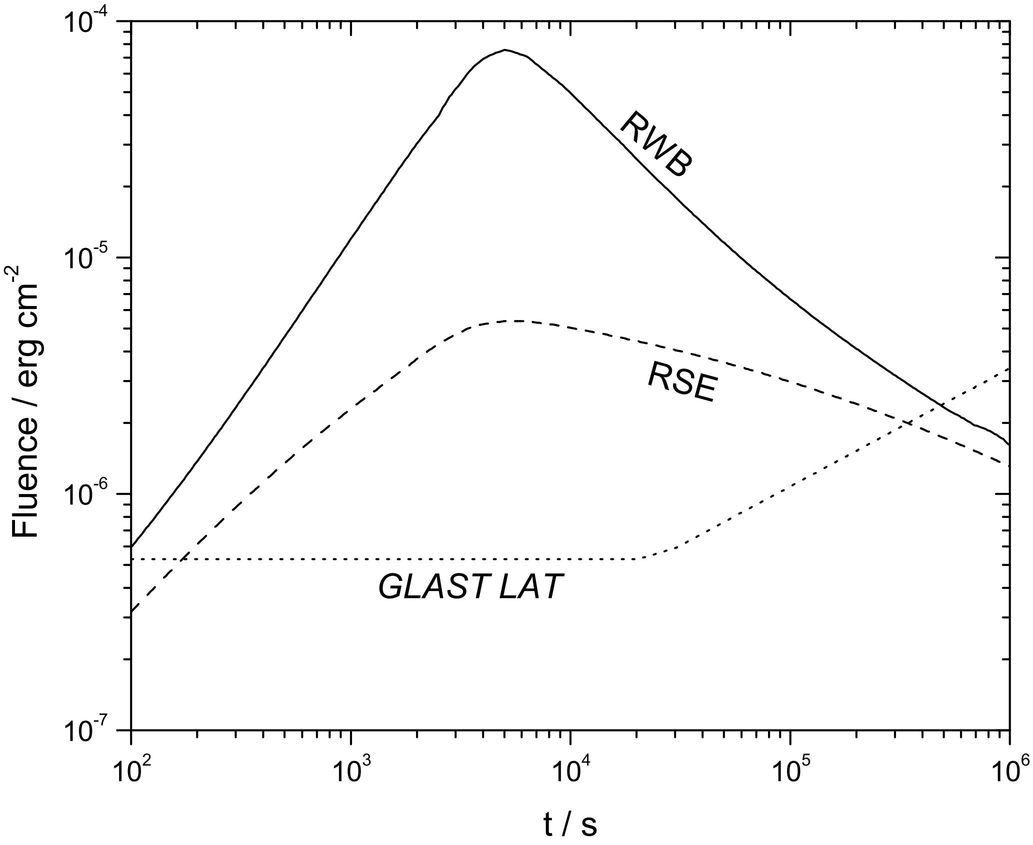

Fig. 7.— The partial fluence (defined as $\int_{0.5t}^{t}\int_{\nu_1}^{\nu_2} F_\nu d\nu dt$, where $h\nu_1 = 20$ MeV and $h\nu_2 = 300$ GeV) curves for the RWB and RSE models. The dotted line represents the fluence threshold of the GLAST LAT at 400 MeV.